



## Research articles

## Perpendicular magnetic anisotropy in Co/Pt multilayers induced by hcp-Ho at 400 °C

W.C. Law<sup>a,b</sup>, T.L. Jin<sup>a</sup>, X.T. Zhu<sup>b</sup>, R.R. Nistala<sup>b</sup>, N. Thiyagarajah<sup>b</sup>, C.S. Seet<sup>b</sup>, W.S. Lew<sup>a,\*</sup><sup>a</sup> School of Physical and Mathematical Sciences, Nanyang Technological University, Singapore 637371, Singapore<sup>b</sup> GLOBALFOUNDRIES Singapore Pte, Ltd., Singapore 738406, Singapore

## A B S T R A C T

In this study, we report that perpendicular magnetic anisotropy (PMA) in Co/Pt multilayers can be achieved by using hcp-Ho(1 0 0) as the seed layer after annealing at 400 °C. M-H hysteresis loops show that the annealing duration required to achieve optimal PMA in Co/Pt multilayers increases monotonically with the Ho seed layer thickness. XRD measurements reveal that Ho transits from amorphous state to hcp structure after annealing at 400 °C, leading to the formation of fcc-Co/Pt (1 1 1). A larger retention of saturation magnetization is also observed when Ho is used as the seed layer as compared to Ru or Pt, which is ascribed to the suppression of interlayer diffusion. This can be attributed to the large grain size of Ho based on the full-width-half-maximum (FWHM) of the Ho peak from XRD results. Synthetic antiferromagnetic (SAF) structures using Ho as a seed layer also demonstrated an exchange coupling strength of  $J_{ex} \approx 1.05$  erg/cm<sup>2</sup> when the thickness of the Ru coupling layer is 0.4 nm.

## 1. Introduction

Magnetoresistive Random Access Memory (MRAM) has been recognized as the most promising emerging non-volatile memory (NVM) technology due to its fast read/write speed, potential for scalability, high endurance and compatibility with CMOS technology [1–3]. Research focus has been directed towards using magnetic materials with perpendicular magnetic anisotropy (PMA) to fabricate perpendicular Magnetic Tunnel Junctions (pMTJ), which is the storage element at the core of the MRAM device. One of the important criteria for MRAM applications is that the pMTJ stack must have the thermal budget to withstand 400 °C annealing temperature in order to integrate with CMOS-BEOL processes [4–7].

Multilayers consisting of multiple bilayer repeats such as Co/Ni, Co/Pt and Co/Pd are attractive candidates as reference layer as their magnetic and material properties can be tuned with ease [8–15]. Among which, Co/Pt is commonly deployed within the industry as it exhibits a wide process margin in retaining high PMA even after 400 °C annealing [14–18]. The origin of PMA within Co/Pt multilayers arises from magnetocrystalline anisotropy (MCA) as well as interfacial effect, which is dependent on the underlying seed layer [18–22]. However, significant interlayer diffusion may occur during 400 °C annealing, resulting in a detrimental impact on the saturation magnetization ( $M_s$ ) or PMA of Co/Pt multilayers [15]. Therefore, the seed layer should ideally have low surface roughness or large grain size while being able to promote the growth of fcc-Co/Pt(1 1 1) responsible for MCA [16]. The

seed layer should also be as thin as possible to maintain low aspect ratio as well as to minimize re-deposition during etching [23].

The corresponding seed layer candidates for Co/Pt multilayers are usually Ru and Pt, as they have been demonstrated to promote the necessary crystallographic texture that retains PMA even after 400 °C for at least 30 min [16–18]. Thick Pt seed layer is desirable to achieve high PMA in Co/Pt multilayers [19,20], but is typically reduced for practicality in the fabrication of pMTJ devices. In addition, Pt, being a noble metal, may pose a challenge when reactive ion etching (RIE) is used for fast throughput [17,24–26]. On the other hand, the re-deposition when etching Ru may remain conductive even after post-etch surface treatment via oxidation.

Holmium (Ho) is theoretically able to achieve hcp-phase upon annealing at 400 °C [27,28]. Since Ho has a lower melting point of 1470 °C, the grain size should be larger as compared to Ru and Pt seed layers, which in turn leads to fewer grain boundaries for interlayer diffusion to occur [29,30]. Based on the fitting of X-ray reflectometry (XRR) (see Supplementary Figure S3), Ho appears to be affected by natural oxidation to some extent reveals that 1.37 out of 52.48 nm of Ho is oxidized. This corresponds to a sheet resistance  $R_s$  of 35.11 Ω/square from four-point probe measurements, which is approximately twice the value of theoretical resistivity  $\rho$  for bulk Ho according to the relation  $\rho = R_s t$ , where  $t = 52.48$  nm is the thickness of Ho. For comparison, the surface oxidation for Pt, Ru and Ta are 1.18, 1.50 and 2.43 nm, respectively. Under controlled environment (e.g. in high vacuum RIE chamber with *in-situ* encapsulation), such highly resistive

\* Corresponding author.

E-mail address: [WenSiang@ntu.edu.sg](mailto:WenSiang@ntu.edu.sg) (W.S. Lew).<https://doi.org/10.1016/j.jmmm.2019.01.023>

Received 12 November 2018; Received in revised form 27 December 2018; Accepted 6 January 2019

Available online 14 January 2019

0304-8853/ © 2019 Elsevier B.V. All rights reserved.

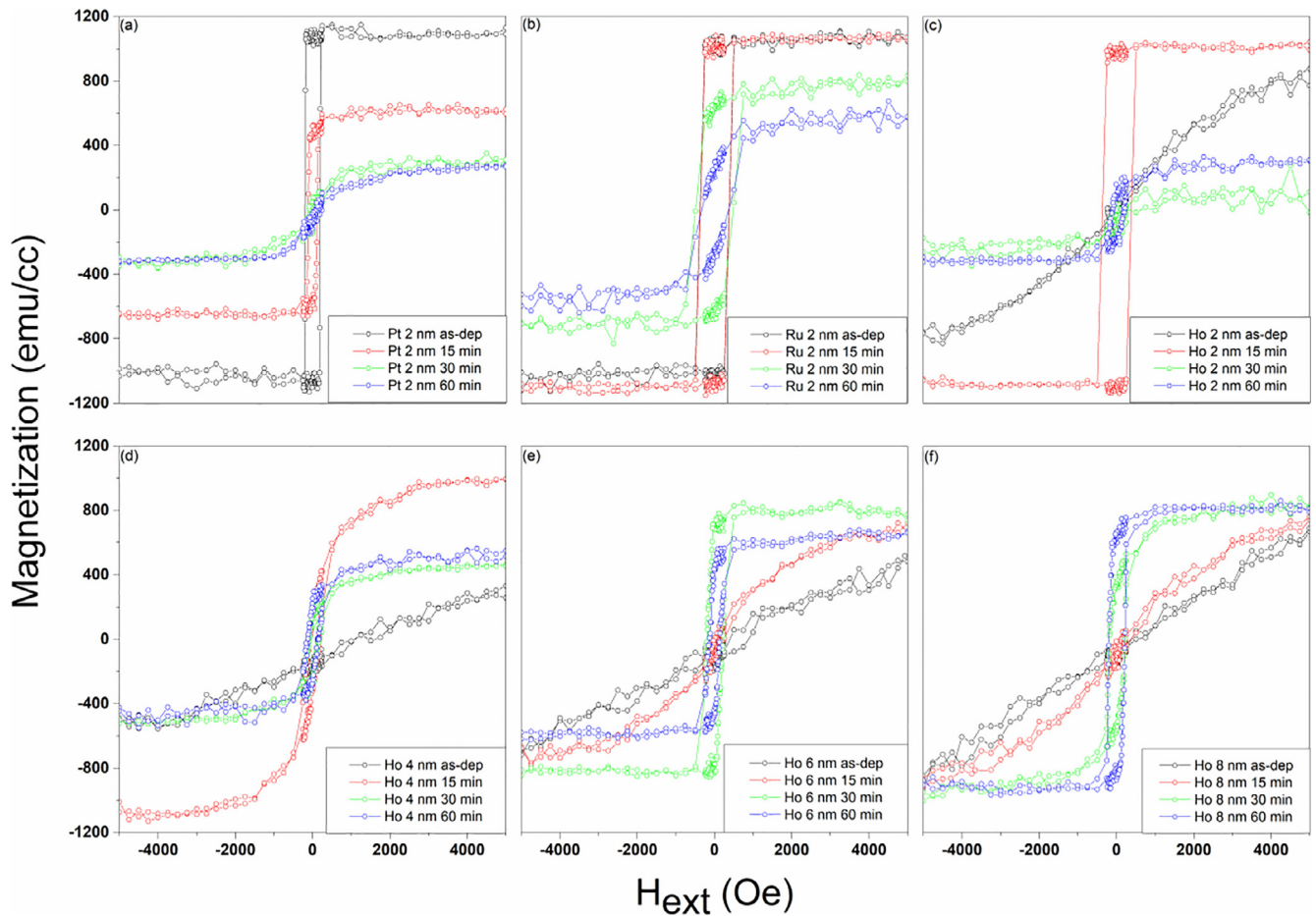


**Fig. 1.** Out-of-plane M-H hysteresis results based from the annealing duration study of Si / SiO<sub>2</sub> / Ta(5) / X / [Co(0.6) / Pt(0.4)]<sub>4</sub> / Ta(5), where X is the seed layer chosen to be (a) 2 nm of Pt, (b) 2 nm of Ru, and (c-f) Ho as seed layer with nominal thicknesses chosen to be 2, 4, 6 and 8 nm respectively. Black, red, green and blue lines for all samples correspond to as-deposited, 15 min, 30 min and 60 min of annealing at 400 °C, respectively. (For interpretation of the references to colour in this figure legend, the reader is referred to the web version of this article.)

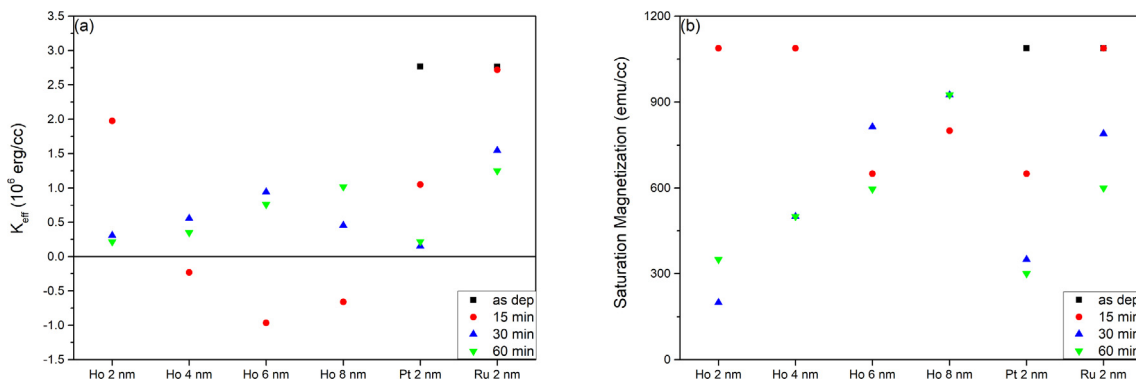


**Fig. 2.** Summary plot of (a)  $K_{eff}$  and (b)  $M_s$  as a function of different seed layers under different annealing duration.

Rare Earth Oxide could offer some relief to the issue of sidewall redeposition. With the Spin Hall Angle (SHA) estimated to have a lower bound value of 0.14 [31], Ho could be a potential candidate for generating spin current through the Spin Hall Effect. These aforementioned characteristics of Ho could therefore provide an interesting alternative as a seed layer for pMTJ.

In this paper, we have explored the effect of Ho as an ultrathin seed layer on the magnetic properties of Co/Pt multilayers and synthetic antiferromagnetic (SAF) structures. The range of PMA obtained ( $K_{eff} \approx 1 \times 10^6$  erg/cc) is comparable to samples with conventional seed layers upon annealing at 400 °C for various durations. This is attributed to the

formation of fcc-Co/Pt peaks after post annealing at 400 °C induced by the recrystallization of Ho as it transits towards hcp-phase. The exchange coupling strength of  $J_{ex}$  is also calculated to be 1.05 erg/cm<sup>2</sup> when 0.4 nm of Ru is used as the coupling layer in the SAF structure.

## 2. Methodology

The samples are prepared using research grade magnetron sputtering system with a base pressure lower than  $6 \times 10^{-8}$  Torr similar to previous works [32,33]. The sputter power and working pressure of Ar plasma are maintained at 50 Watts and 2 mTorr, respectively. Two sets

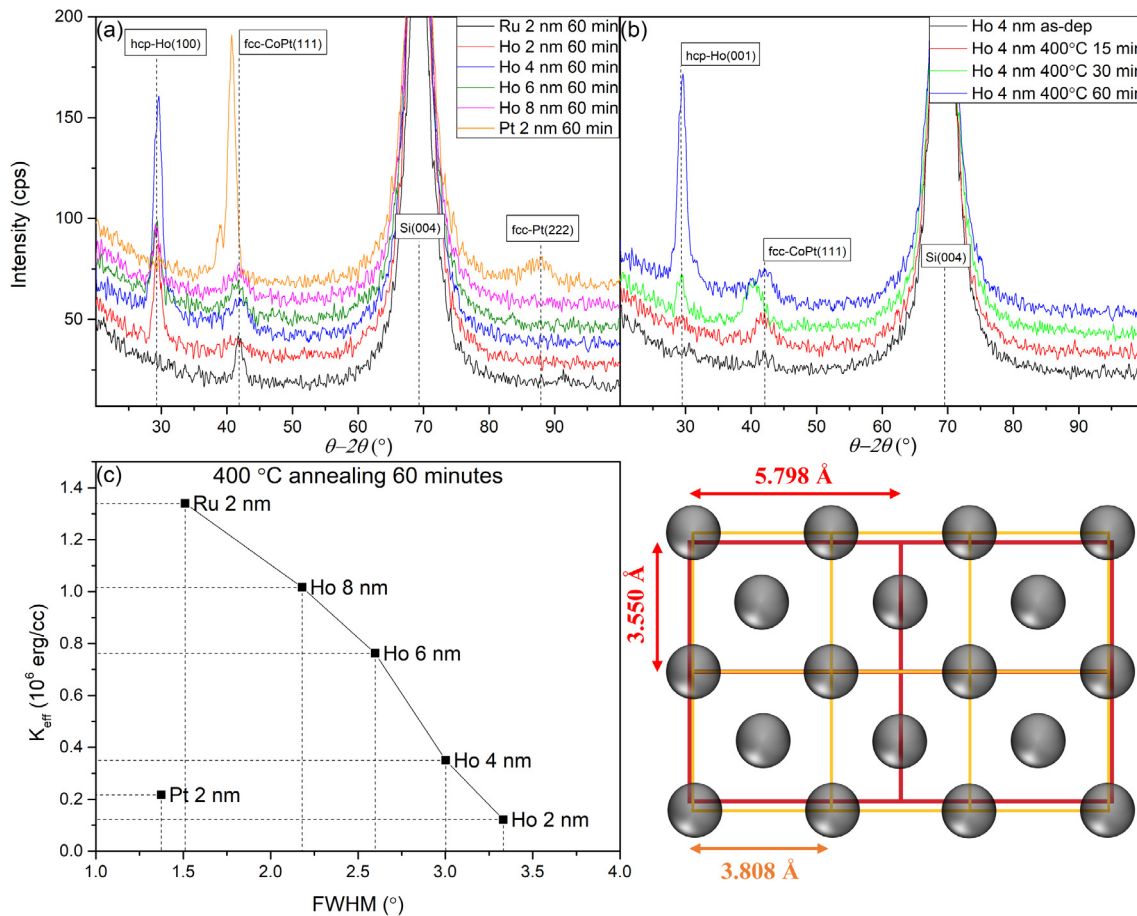


**Fig. 3.**  $\theta$ - $2\theta$  XRD scans for selected samples with (a) Si / SiO<sub>2</sub> / Ta(5) / X / [Co(0.6) / Pt(0.4)]<sub>4</sub> / Ta(5) annealed at 400 °C for an hour, where X is seed layer such as Pt (2), Ru(2) and Ho of varying thicknesses, (b) Si / SiO<sub>2</sub> / Ta(5) / Ho(4) / [Co(0.6) / Pt(0.4)]<sub>4</sub> / Ta(5) in the as-deposited state and annealed at 400 °C for various duration. Constant vertical offset of 10 counts-per-second (cps) and Savitzky–Golay filter of 5 averaging points are applied for clarity. (c) FWHM of Co/Pt peaks from XRD results as a function of  $K_{eff}$  for samples annealed at 400 °C for an hour. (d) Illustration of fcc-CoPt(1 1 1) lattice (in orange squares with  $a_{CoPt} = 3.81 \text{ \AA}$  and Co atoms as black spheres) overlaying the hcp-Ho(1 0 0) plane (in red rectangles with  $a_{Ho} = 3.55 \text{ \AA}$  and  $c_{Ho} = 5.798 \text{ \AA}$ ). (For interpretation of the references to colour in this figure legend, the reader is referred to the web version of this article.)

of thin film samples are deposited on thermally oxidized silicon substrates as detailed below, with numbers within the parenthesis referring to nominal thickness in nm, i.e.

- (A) Si / SiO<sub>2</sub> / Ta(5) / X / [Co(0.6) / Pt(0.4)]<sub>4</sub> / Ta(5), where X is the seed layer chosen to be Pt(2), Ru(2) and Ho with thickness  $t_{Ho} = 2, 4, 6$  and 8 nm, and
- (B) Si / SiO<sub>2</sub> / Ta(5) / Ho(8) / [Co(0.6) / Pt(0.4)]<sub>6</sub> / Co(0.6) / Ru ( $t_{Ru}$ ) / [Co(0.6) / Pt(0.4)]<sub>4</sub> / Co(0.6) / Ta(5), where  $t_{Ru}$  is the nominal thickness of Ru from 0.4 to 0.8 nm.

All films were subsequently diced into 4 mm by 4 mm square samples using an automated dicing tool before being batched annealed at 400 °C for different duration.  $\theta - 2\theta$  scans using X-ray Diffraction (XRD) diffractometer are performed to analyze the crystalline structure of the samples. To obtain the effective anisotropy field  $K_{eff}$  and saturation magnetization  $M_s$ , the magnetic moment of the samples were measured while an external magnetic field of at least 10 kOe is swept in the easy and hard axes using Vibrating Sample Magnetometer (VSM). The easy and hard axes are defined as the magnetic field applied out-of-plane and in-plane with respect to the sample film.  $K_{eff}$  is then determined from the area enclosed within the M-H loops in the easy and hard axes [14,22,34].

### 3. Results and discussion

Fig. 1 shows the M-H loops measured with  $H_{ext}$  applied in the out-of-plane direction for samples with different seed layers undergoing various annealing duration, while Fig. 2 shows the corresponding  $M_s$  and  $K_{eff}$  values extracted from these M-H loops. Hard axis M-H loop measurements where external magnetic field is applied along the film plane exhibit coherent magnetization rotation for all as-deposited and annealed samples (see Supplementary Figure S1). As can be seen from Fig. 1(a), the control sample consisting of 2 nm thickness of Pt seed layer shows complete squareness in the as-deposited state, with  $K_{eff}$  shown in Fig. 2(a) being similar to previous report [28]. When compared to its as-deposited state, the  $K_{eff}$  of Co/Pt multilayers with Pt seed layer degraded by 90% and 70% upon annealing at 400 °C for 30 and 60 min, respectively. As for the sample with Ru seed layer, the  $K_{eff}$  in the as-deposited state for this study as shown in Fig. 2(a) is slightly higher than the sample reported in Fig. 1(b) of reference [14] due to a smaller coercivity ( $H_c \approx 250$  Oe) in the out-of-plane direction. The same degradation effect on  $K_{eff}$  for Ru-based seed layer is observed upon annealing at 400 °C for an hour, except that  $M_s$  also decreases by approximately 50% compared to its as-deposited state. The study of these control samples exemplifies the sensitivity to the stack design and the corresponding changes in the microstructures of the Co/Pt multilayers upon annealing.

On the other hand, Fig. 1(c) to 1(f) reveal an opposite trend from the control samples, where all samples with different thicknesses of Ho as

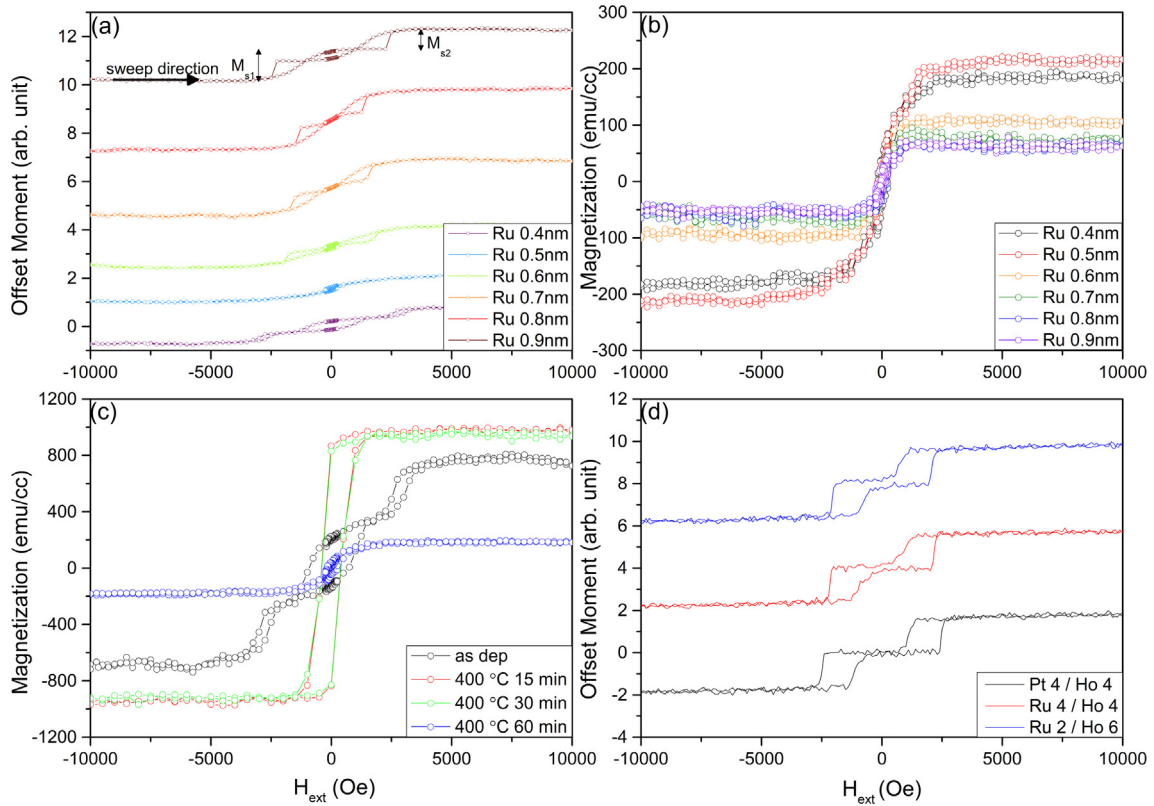


**Fig. 4.** Out-of-plane M-H loops for samples with Si / SiO<sub>2</sub> / Ta(5) / Ho(8) / [Co(0.6) / Pt(0.4)]<sub>6</sub> / Ru(*t*) / [Co(0.6) / Pt(0.4)]<sub>4</sub> / Ta(5), where *t* is the nominal thickness chosen to be from 0.4 to 0.9 nm. (a) Samples in the as-deposited state and (b) samples that underwent 400 °C for an hour. (c) Representative M-H loops of SAF with  $t_{Ru} = 0.4$  nm undergoing different anneal duration. (d) Out-of-plane M-H loops for fully compensated SAF structure consisting of Si / SiO<sub>2</sub> / Ta(5) / X / Ho(4) / [Co(0.6) / Pt(0.4)]<sub>6</sub> / Ru(0.4) / [Co(0.6) / Pt(0.4)]<sub>6</sub> / Ta(5) in the as-deposited state, where X is Pt or Ru as described in the legend.

seed layer show in-plane magnetic anisotropy (IMA) in the as-deposited state. PMA is gradually observed as the annealing duration increases alongside with the thickness of Ho seed layer, which is ascribed to the transition towards hcp-Ho(100) that can promote fcc-CoPt(111) growth. This is evident from XRD results as shown in Fig. 3(b), where no significant peaks for Ho and fcc-CoPt are observed when the sample with 4 nm of Ho as the seed layer is in the as-deposited state. Upon annealing at 400 °C for longer duration, peaks at 29° and 42° are observed, which correspond to hcp-Ho(100) and fcc-CoPt(111), respectively. We reasoned that annealing at 400 °C is not the cause of fcc-CoPt(111) formation, as the same degree of PMA should otherwise exist for all samples with a set amount of annealing duration, i.e. the same sharp switching observed in Fig. 1(c) after 15 min of annealing should also occur for other samples if Ho had zero influence on the formation of fcc-CoPt(111). Instead, the formation of fcc-CoPt(111) relies heavily on the choice of underlying seed layer, as exemplified by the case of amorphous Ho or Mo as the seed layer (see Supplementary Figure S2).

Therefore, we propose that the crystallization of hcp-Ho(100) is responsible for the growth of fcc-CoPt(111), as the thickness of the Ho seed layer is the only variable within these samples. The interplay between the annealing duration and the evolution of the M-H loops can be explained by the crystallization rate of Ho, *k*, based on the Arrhenius model;

$$k = \frac{E_a}{RT} \quad (1)$$

where  $E_a$  is the activation energy, *R* is the gas constant and *T* is the annealing temperature. While *k* is typically expressed in mol/seconds, we denote the areal crystallization rate  $k_A$  to be nm per minute (nm/min) since the lateral dimensions of the sample die are constant, i.e. 4 mm by 4 mm square dies. Therefore, when samples with Ho > 2 nm

of seed layer are subjected to only 15 min of annealing, the incomplete crystallization of Ho will not be adequate to form a template for fcc-CoPt growth, resulting in negative  $K_{eff}$  values as shown in Fig. 2(a). Base on the optimal  $K_{eff}$  values for each Ho thickness from Fig. 2(a),  $k_A$  is determined to be 0.1333 nm/min. As shown in Supplementary Figure S1(q), a new sample with 10 nm of Ho thickness confirms the linear relation between  $t_{Ho}$  and annealing duration as it is able to achieve  $K_{eff} = 1.389 \times 10^6$  erg/cc when annealed for 75 min, which is consistent with previous samples.

The plots of  $K_{eff}$  and  $M_s$  as a function of various seed layers and annealing duration are summarized in Fig. 2(a) and (b).  $M_s$  is observed to decrease for all samples upon annealing, which can be attributed to interlayer mixing between interfaces [14]. Indeed, the  $M_s$  in this study is obtained by dividing the areal moment with the nominal thickness of total Co deposited in our multilayer structure without accounting for interlayer diffusion. However, in the case of samples with Ru as the seed layer, the overall high  $K_{eff}$  value is due to the increase in  $H_k$  from 5 kOe to 10 kOe as observed in hard axis measurements. For samples with Ho and Pt as the seed layer, the  $H_k$  values from in-plane M-H loops are similar at 5 kOe after annealing. These observations are congruent with the fcc-CoPt(111) peaks extracted from XRD as shown in Fig. 3(a). While the fcc-Co/Pt(111) peak intensities are similar across different samples, the full-width-half-maximums (FWHMs) of Co/Pt multilayer peaks for samples with Pt and Ru-based seed layers at their optimal  $H_k$  are at around 1.5°, which is comparable to previous report [17]. On the other hand, the FWHMs of Co/Pt multilayers for samples with Ho-based seed layers after annealing are approximately 3.5°. This could be due to a large lattice mismatch between Ho and Co similar to Hf seed layer, whereas Ru and Pt seed layers have lower lattice mismatch at 8% and 9%, respectively [17,35]. Fig. 3(d) illustrates the periodic arrangement of fcc-Co/Pt(111) above hcp-Ho(100). Base on the interplanar *d*-

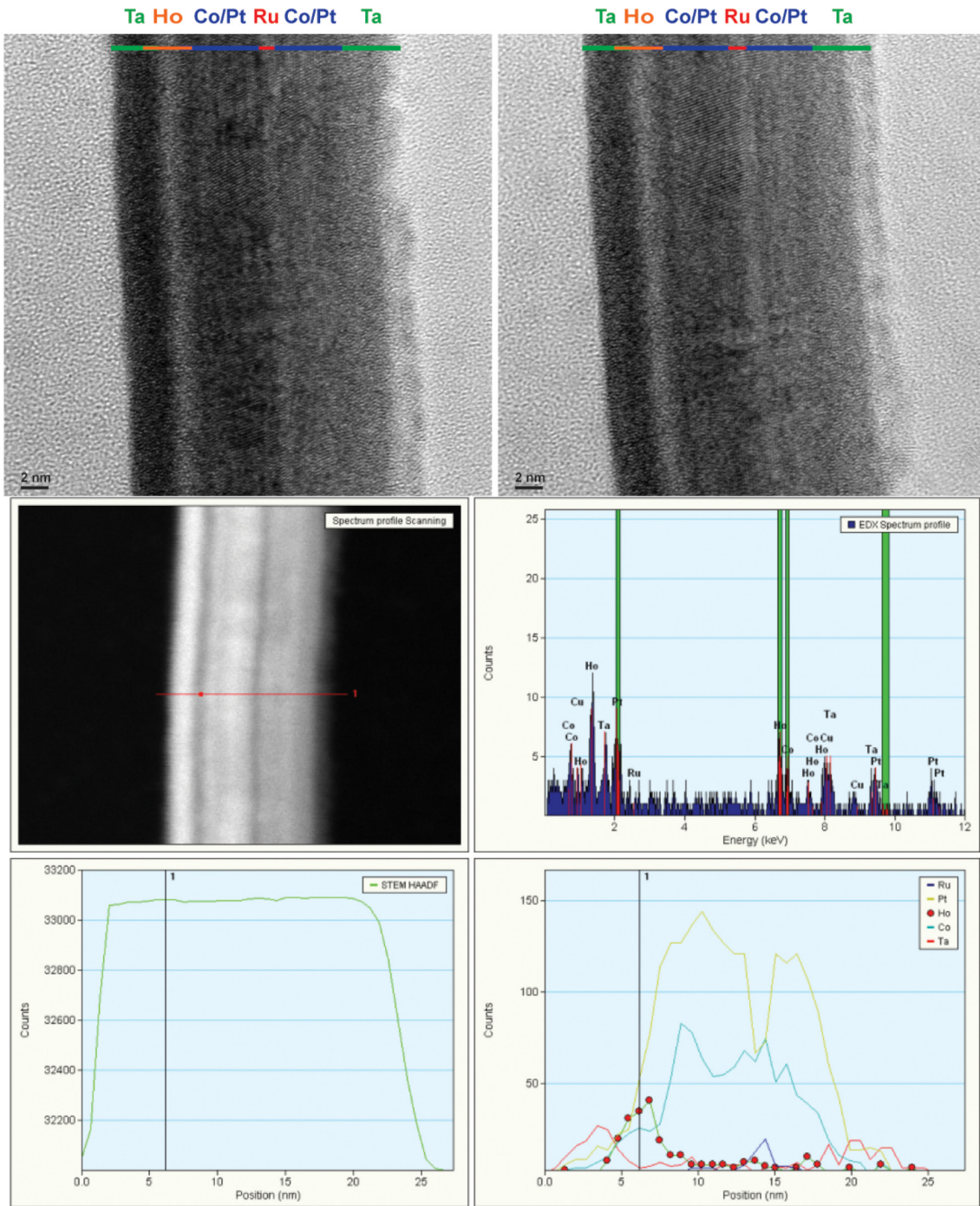


Fig. 5. TEM image and EDX line scan profile of Si / SiO<sub>2</sub> / Ta(5) / Ho(8) / [Co(0.6) / Pt(0.4)]<sub>6</sub> / Co(0.6) / Ru (0.8) / [Co(0.6) / Pt(0.4)]<sub>4</sub> / Co(0.6) / Ta(5) in the as-deposited state.

spacing of 3.075 Å obtained from XRD results, the lattice constants of hcp-Ho are determined to be  $a_{Ho} = 3.551$  Å and  $c_{Ho} = 5.798$  Å, close to theoretical values [36]. On the other hand, for fcc-CoPt with a  $d$ -spacing of 2.198 Å, the lattice constant  $a_{CoPt}$  would be 3.808 Å. Therefore, one may expect that strained growth is induced due to the lattice mismatch along the  $c$ -axis of Ho, resulting in a larger FWHM of the Co/Pt peak from XRD results. The FWHM of fcc-CoPt(1 1 1) peaks determined from Gaussian fitting of the XRD results are plotted against the  $K_{eff}$  of the samples annealed at 400 °C for an hour, as shown in Fig. 3(c). As with previous references, we can correlate that the quality of the peaks is crucial to achieve high PMA in Co/Pt multilayers [17,28].

Despite fcc-Co/Pt(1 1 1) peaks having a wider FWHM for samples

with Ho as seed layers, the PMA remains relatively high across different Ho thicknesses due to a lower decrease in  $M_s$  as shown in Fig. 2(b). This can be attributed to the suppression of interlayer mixing between Co and Ta due to a large grain size for Ho, which is calculated to be  $D = 5.612$  nm based on the Scherrer's equation,

$$D = \frac{K\lambda}{FWHM \times \cos \theta} \quad (2)$$

where  $K = 0.94$  is the Scherrer's constant,  $\lambda = 1.5406$  Å is the x-ray wavelength of Cu  $K\alpha_1$  and  $\theta = 0.257$  rad is the Bragg's angle. A lack of Ru peak from XRD measurement impedes a quantitative comparison, but it has been shown to be an effective diffusion barrier against Ta in

our previous work [30]. Therefore, the larger post-annealing  $M_s$  seen in samples with Ru or Ho seed layers in contrast to the sample with Pt seed layer is due to a reduction in intermixing between Co and the Ta bottom electrode.

In addition, SAF structure is commonly deployed in pMTJ in order to reduce the stray field arising from the reference layer that may induce magnetostatic coupling with the free layer. SAF structure can also be of technological importance in other spintronics applications such as skyrmions and domain wall propagation, in which Ho could also serve as a SOT-write line and seed layer [37–41]. Therefore, SAF structures are investigated using 8 nm of Ho as seed layer with varying thicknesses of Ru as the exchange coupling layer. Fig. 4(a) shows the M-H hysteresis loops for samples in the as-deposited state, while all samples that underwent annealing revealed a single switching state as shown in Fig. 4(b) and (c).

The exhibition of PMA in the as-deposited state seen in Fig. 4(a) may seem to contradict with results from Fig. 1(c-f), where samples with Ho as the seed layer are required to be annealed at 400 °C in order to induce growth for fcc-Co/Pt. However, Transmission Electron Microscopy (TEM) analysis as shown in Fig. 5(a) and (b) reveals that Ho indeed is in an amorphous state, further validating the XRD results of the as-deposited samples, while the SAF structure is polycrystalline in the fcc-phase. The crystallization appears to originate from the Ru coupling layer, which explains the intermediate switching state of the SAF structure with  $t_{Ru} = 0.4$  nm, as  $K_{eff}$  of the underlying [Co/Pt]<sub>6</sub> multilayers would most likely to be weaker than the first peak Ru exchange coupling  $J_{ex}$ . Since the Ru coupling layer could not exert a strong influence on the crystallization of [Co/Pt]<sub>6</sub> as much as [Co/Pt]<sub>4</sub>, the  $M_s$  of the SAF in the as-deposited state is not fully saturated even at 10 kOe as shown in Fig. 4(c). Another proof that [Co/Pt]<sub>6</sub> is unable to achieve high PMA comes from the M-H loop for sample with  $t_{Ru} = 0.8$  nm, where the magnetic moment switching at  $M_{s1}$  is larger than the moment at  $M_{s2}$  as indicated in Fig. 4(a). As shown in Fig. 4(d), we are able to eliminate such intermediate switching state in subsequent stack development by using an equal number of [Co/Pt] bilayer repeats to fully compensate any stray field, as well as the usage of Ru / Ho or Pt / Ho as the composite seed layer. Nonetheless, the anti-ferromagnetic coupling still disappeared after 400 °C of annealing in the same manner as Fig. 4(c), suggesting that the root cause would lie in the diffusion of Ru coupling layer that causes pinhole formation. It is well known that such pinhole formation will lead to ferromagnetic coupling that can dominate the effect induced by interlayer exchange coupling [42,43].

The exchange coupling of SAF using 1st peak Ru in the as-deposited state is also estimated for completeness. According to the equation  $J_{ex} = H_{ex}M_s t$ , where  $J_{ex}$  is the exchange coupling strength,  $H_{ex}$  denotes the interlayer coupling field,  $t$  denotes the thickness of the softer multilayer and  $M_s$  is the saturation magnetization, if we assume the  $M_s$  of the as-deposited Co to be 1088 emu/cc as per Figs. 1 and 4(c),  $J_{ex}$  induced from the 1st peak Ru would be  $\approx 1.05$  erg/cm<sup>2</sup>. This value would be in the same order of magnitude as reported in literature [42,44].

#### 4. Conclusion

In conclusion, we have demonstrated that Ho is able to induce perpendicular magnetic anisotropy for Co/Pt multilayers after its transition into hcp-phase.  $K_{eff} \approx 2.013 \times 10^6$  erg/cc can be achieved for Ho seed layers with different thickness and annealing duration at 400 °C, which is comparable to samples with Pt and Ru seed layers. XRD analysis reveals the hcp-Ho and fcc-Co/Pt are only activated with 400 °C annealing as evident by peaks observed at 29° and 42°. Moreover, a larger Ho grain size may help to suppress interlayer mixing, which accounts for the higher  $M_s$  in comparison to Pt and Ru seed layers. An exchange coupling strength of 1.05 erg/cm<sup>2</sup> is also obtained for a SAF structure with 0.4 nm of Ru used as a coupling layer.

#### Acknowledgements

The work was supported by the Singapore National Research Foundation, Prime Minister's Office under a Competitive Research Programme (Non-volatile Magnetic Logic and Memory Integrated Circuit Devices, NRF-CRP9-2011-01), and an Industry-IHL Partnership Program (NRF2015-IIP001-001). The support from an RIE2020 AME-Programmatic Grant (No. A1687b0033) and an IAF-ICP Grant (No. I1801E0030) is also acknowledged. WSL is also a member of the Singapore Spintronics Consortium (SG-SPIN).

#### Appendix A. Supplementary data

Supplementary data to this article can be found online at <https://doi.org/10.1016/j.jmmm.2019.01.023>.

#### References

- [1] E. Chen, D. Apalkov, Z. Diao, A. Driskill-Smith, D. Druist, D. Lottis, V. Nikitin, X. Tang, S. Watts, S. Wang, S.A. Wolf, A.W. Ghosh, J.W. Lu, S.J. Poon, M. Stan, W.H. Butler, S. Gupta, C.K.A. Mewes, T. Mewes, P.B. Visscher, Advances and Future Prospects of Spin-Transfer Torque Random Access Memory, *IEEE Trans. Magn.* 46 (6) (2010) 1873–1878.
- [2] R. Sbiaa, H. Meng, S.N. Piramanayagam, Materials with perpendicular magnetic anisotropy for magnetic random access memory, *physica status solidi (RRL) Rapid Res. Lett.* 5 (12) (2011) 413–419.
- [3] H. Ohmori, T. Hatori, S. Nakagawa, “Perpendicular magnetic tunnel junction with tunneling magnetoresistance ratio of 64% using MgO (100) barrier layer prepared at room temperature,” (in English), *J. Appl. Phys.* 103 (7) (2008) 07A911.
- [4] S.-E. Lee, Y. Takemura, J.-G. Park, Effect of double MgO tunneling barrier on thermal stability and TMR ratio for perpendicular MTJ spin-valve with tungsten layers, *Appl. Phys. Lett.* 109 (18) (2016).
- [5] S.-E. Lee, T.-H. Shim, J.-G. Park, Perpendicular magnetic tunnel junction (p-MTJ) spin-valves designed with a top Co2Fe6B2 free layer and a nanoscale-thick tungsten bridging and capping layer, *NPG Asia Mater.* 8 (11) (2016).
- [6] S. Couet, J. Swerts, S. Mertens, T. Lin, Y. Tomczak, E. Liu, B. Douhard, S. Van Elshocht, A. Furnemont, G.S. Kar, Oxygen Scavenging by Ta Spacers in Double-MgO Free Layers for Perpendicular Spin-Transfer Torque Magnetic Random-Access Memory, *IEEE Magn. Lett.* 7 (2016) 1–4.
- [7] S. Couet, T. Devolder, J. Swerts, S. Mertens, T. Lin, E. Liu, S.V. Elshocht, G.S. Kar, Impact of Ta and W-based spacers in double MgO STT-MRAM free layers on perpendicular anisotropy and damping, *Appl. Phys. Lett.* 111 (15) (2017) 152406.
- [8] R. Law, R. Sbiaa, T. Liew, T.C. Chong, Effects of Ta seed layer and annealing on magnetoresistance in Co Fe/ Pd-based pseudo-spin-valves with perpendicular anisotropy, *Appl. Phys. Lett.* 91 (24) (2007) 242504.
- [9] R. Law, R. Sbiaa, T. Liew, T.C. Chong, Magnetoresistance and switching properties of Co-Fe/Pd-based perpendicular anisotropy single-and dual-spin valves, *IEEE Trans. Magn.* 44 (11) (2008) 2612–2615.
- [10] E. Liu, J. Swerts, T. Devolder, S. Couet, S. Mertens, T. Lin, V. Spampinato, A. Franquet, T. Conard, S. Van Elshocht, Seed layer impact on structural and magnetic properties of [Co/Ni] multilayers with perpendicular magnetic anisotropy, *J. Appl. Phys.* 121 (4) (2017) 043905.
- [11] G. Kar, W. Kim, T. Tahmasebi, J. Swerts, S. Mertens, N. Heylen, T. Min, Co/Ni based p-MTJ stack for sub-20nm high density stand alone and high performance embedded memory application, in: *Electron Devices Meeting (IEDM), 2014 IEEE International*, 2014, pp. 1–4: IEDM14-479.
- [12] M. Gottwald, K. Lee, J. Kan, B. Ocker, J. Wrona, S. Tibus, J. Langer, S. Kang, E. Fullerton, Ultra-thin Co/Pd multilayers with enhanced high-temperature annealing stability, *Appl. Phys. Lett.* 102 (5) (2013) 052405.
- [13] H. Kurt, M. Venkatesan, J. Coey, Enhanced perpendicular magnetic anisotropy in Co/Ni multilayers with a thin seed layer, *J. Appl. Phys.* 108 (7) (2010) 073916.
- [14] T. Young Lee, D. Su Son, S. Ho Lim, S.-R. Lee, High post-annealing stability in [Pt/Co] multilayers, vol. 113, no. 216102, pp. 1–3, 2013.
- [15] S. Bandiera, R. Sousa, B. Rodmacq, B. Dieny, Enhancement of perpendicular magnetic anisotropy through reduction of Co-Pt interdiffusion in (Co/Pt) multilayers, *Appl. Phys. Lett.* 100 (14) (2012) 142410.
- [16] M. Gottwald, J. Kan, K. Lee, X. Zhu, C. Park, S. Kang, Scalable and thermally robust perpendicular magnetic tunnel junctions for STT-MRAM, *Appl. Phys. Lett.* 106 (3) (2015) 032413.
- [17] J. Chatterjee, T. Tahmasebi, S. Mertens, G.S. Kar, T. Min, J. De Boeck, Seed layer effect on the magnetic properties of ultrathin Co/Pt multilayers with perpendicular magnetic anisotropy, *IEEE Trans. Magn.* 50 (11) (2014) 1–4.
- [18] K. Yakushiji, T. Saruya, H. Kubota, A. Fukushima, T. Nagahama, S. Yuasa, K. Ando, Ultrathin Co/Pt and Co/Pd superlattice films for MgO-based perpendicular magnetic tunnel junctions, *Appl. Phys. Lett.* 97 (23) (2010) 232508.
- [19] C.-J. Lin, G. Gorman, C. Lee, R. Farrow, E. Marinero, H. Do, H. Notarys, C. Chien, Magnetic and structural properties of Co/Pt multilayers, *J. Magn. Magn. Mater.* 93 (1991) 194–206.
- [20] S. Tang, P. Carcia, D. Coulman, A. McGhie, Scanning tunneling microscopy of Pt/Co multilayers on Pt buffer layers, *Appl. Phys. Lett.* 59 (22) (1991) 2898–2900.

- [21] G. Bertero, R. Sinclair, Structure-property correlations in Pt/Co multilayers for magneto-optic recording, *J. Magn. Magn. Mater.* 134 (1) (1994) 173–184.
- [22] S.T. Lim, M. Tran, J.W. Chenchen, J.F. Ying, G. Han, Effect of different seed layers with varying Co and Pt thicknesses on the magnetic properties of Co/Pt multilayers, *J. Appl. Phys.* 117 (17) (2015) 17A731.
- [23] W. Boullart, D. Radisic, V. Paraschiv, S. Cornelissen, M. Manfrini, K. Yatsuda, E. Nishimura, T. Ohishi, S. Tahara, STT MRAM patterning challenges, in *Advanced Etch Technology for Nanopatterning II*, 2013, vol. 8685, p. 86850F: International Society for Optics and Photonics.
- [24] E.H. Kim, Y.B. Xiao, S.M. Kong, C.W. Chung, Investigation on etch characteristics of nanometer-sized magnetic tunnel junction stacks using a HBr/Ar plasma, *J. Nanosci. Nanotechnol.* 11 (7) (2011) 6616–6620.
- [25] E.H. Kim, T.Y. Lee, C.W. Chung, Evolution of etch profile of magnetic tunnel junction stacks etched in a CH<sub>3</sub>OH/Ar plasma, *J. Electrochem. Soc.* 159 (3) (2012) H230–H234.
- [26] L. Cuchet, B. Rodmacq, S. Auffret, R.C. Sousa, I.L. Prejbeanu, B. Dieny, Perpendicular magnetic tunnel junctions with a synthetic storage or reference layer: A new route towards Pt- and Pd-free junctions, *Sci. Rep.* 6 (2016) 21246.
- [27] G. Cacciamani, S. De Negri, A. Saccone, R. Ferro, The Al–R–Mg (R = Gd, Dy, Ho) systems. Part II: thermodynamic modelling of the binary and ternary systems, *Intermetallics* 11 (11–12) (2003) 1135–1151.
- [28] P. Garcia, M. Reilly, Z. Li, H. van Kesteren, Ar-sputtered Pt/Co multilayers with large anisotropy energy and coercivity, *IEEE Trans. Magn.* 30 (6) (1994) 4395–4397.
- [29] M.A. Nicolet, Diffusion barriers in thin films, *Thin Solid Films* 52 (1978) 415–443.
- [30] W.C. Law, T. Tahmasebi, F. Tan, T. Jin, W. Gan, X. Zhu, Z.Q. Mo, H.W. Teo, C.S. Seet, A. See, High temperature Ferromagnetic Resonance study on pMTJ stacks with diffusion barrier layers, *J. Phys. D Appl. Phys.* 51 (405001) (2018) 1–7.
- [31] N. Reynolds, P. Jadaun, J.T. Heron, C.L. Jermain, J. Gibbons, R. Collette, R. Buhrman, D. Schlom, D. Ralph, Spin Hall torques generated by rare-earth thin films, *Phys. Rev. B* 95 (6) (2017) 064412.
- [32] F. Tan, G. Lim, W. Law, F. Luo, H. Liu, F. Poh, D. Shum, W. Lew, Electric field control on gated Pt/Co/SiO<sub>2</sub> heterostructure with insulating polymer, *J. Phys. D Appl. Phys.* 51 (36) (2018) 365001.
- [33] F. Luo, S. Goolaup, W.C. Law, S. Li, F. Tan, C. Engel, T. Zhou, W.S. Lew, Simultaneous determination of effective spin-orbit torque fields in magnetic structures with in-plane anisotropy, *Phys. Rev. B* 95 (2017) 174415.
- [34] J.H. Jung, S.H. Lim, S.-R. Lee, Perpendicular magnetic anisotropy properties of CoFeB/Pd multilayers, *J. Nanosci. Nanotechnol.* 11 (7) (2011) 6233–6236.
- [35] J. Chatterjee, T. Tahmasebi, J. Swerts, G.S. Kar, J. De Boeck, Impact of seed layer on post-annealing behavior of transport and magnetic properties of Co/Pt multilayer-based bottom-pinned perpendicular magnetic tunnel junctions, *Appl. Phys. Express* 8 (6) (2015) 063002.
- [36] F.H. Spedding, A. Daane, K. Herrmann, The crystal structures and lattice parameters of high-purity scandium, yttrium and the rare earth metals, *Acta Crystallographica* 9 (7) (1956) 559–563.
- [37] W.L. Gan, S. Krishnia, W.S. Lew, Efficient in-line skyrmion injection method for synthetic antiferromagnetic systems, *New J. Phys.* 20 (1) (2018) 013029.
- [38] X. Zhang, Y. Zhou, M. Ezawa, Magnetic bilayer-skyrmions without skyrmion Hall effect, *Nat. Commun.* 7 (2016) 10293.
- [39] S.-H. Yang, K.-S. Ryu, S. Parkin, Domain-wall velocities of up to 750 m s<sup>-1</sup> driven by exchange-coupling torque in synthetic antiferromagnets, *Nat. Nanotechnol.* 10 (3) (2015) 221.
- [40] Z. Yu, Y. Zhang, Z. Zhang, M. Cheng, Z. Lu, X. Yang, J. Shi, R. Xiong, Domain-wall motion at an ultrahigh speed driven by spin-orbit torque in synthetic antiferromagnets, *Nanotechnology* 29 (17) (2018) 175404.
- [41] Z. Meng, S. He, L. Huang, J. Qiu, T. Zhou, C. Panagopoulos, G. Han, K.-L. Teo, Current induced domain wall motion in antiferromagnetically coupled (Co<sub>70</sub>Fe<sub>30</sub>/Pd) multilayer nanowires, *Appl. Phys. Lett.* 109 (14) (2016) 142403.
- [42] K. Yakushiji, H. Kubota, A. Fukushima, S. Yuasa, Perpendicular magnetic tunnel junctions with strong antiferromagnetic interlayer exchange coupling at first oscillation peak, *Appl. Phys. Express* 8 (8) (2015) 083003.
- [43] S. Parkin, D. Mauri, Spin engineering: direct determination of the Ruderman-Kittel-Kasuya-Yosida far-field range function in ruthenium, *Phys. Rev. B* 44 (13) (1991) 7131.
- [44] S. Bandiera, R. Sousa, S. Auffret, B. Rodmacq, B. Dieny, Enhancement of perpendicular magnetic anisotropy thanks to Pt insertions in synthetic antiferromagnets, *Appl. Phys. Lett.* 101 (7) (2012) 072410.